JACS
JOURNAL OF THE AMERICAN CHEMICAL SOCIETY

Communication

pubs.acs.org/JACS

Asymmetric Volcano Trend in Oxygen Reduction Activity of Pt and Non-Pt Catalysts: *In Situ* Identification of the Site-Blocking Effect

Jingkun Li,[†] Amell Alsudairi,[†] Zi-Feng Ma,[‡] Sanjeev Mukerjee,[†] and Qingying Jia*[,†]

[†]Department of Chemistry and Chemical Biology, Northeastern University, Boston, Massachusetts 02115, United States

[‡]Shanghai Electrochemical Energy Devices Research Center, Department of Chemical Engineering, Shanghai Jiao Tong University, Shanghai 200240, China

Supporting Information

ABSTRACT: Proper understanding of the major limitations of current catalysts for oxygen reduction reaction (ORR) is essential for further advancement. Herein by studying representative Pt and non-Pt ORR catalysts with a wide range of redox potential (E_{redox}) via combined electrochemical, theoretical, and *in situ* spectroscopic methods, we demonstrate that the role of the site-blocking effect in limiting the ORR varies drastically depending on the E_{redox} of active sites; and the intrinsic activity of active sites with low E_{redox} have been markedly underestimated owing to the overlook of this effect. Accordingly, we establish a general asymmetric volcano trend in the ORR activity: the ORR of the catalysts on the overly high E_{redox} side of the volcano is limited by the intrinsic activity; whereas the ORR of the catalysts on the low E_{redox} side is limited by either the site-blocking effect and/or intrinsic activity depending on the E_{redox}.

Accelerating the sluggish oxygen reduction reaction (ORR) constitutes a key element in the commercialization of electrochemical energy conversion and storage devices such as fuel cells and metal−air batteries.[1] Platinum is the most efficient element in catalyzing ORR in acidic media, but it is expensive and limited in supply. Its activity can be improved by alloying with transition metals (denoted as PtM, M = Co, Ni, and Cu, *etc.*), leading to lower Pt loading.[2] Progress has also been made in developing nonplatinum (non-Pt) catalysts.[2] The M−N−C materials, which originated from the finding of cobalt phthalocyanine (CoPc) being ORR active in alkaline,[3] have emerged as the leading non-Pt catalysts with the ORR activity approaching that of Pt/C in acidic media.[4] The high activity of Pt and M−N−C catalysts has been unified into the framework of the so-called volcano trend,[5] wherein the ORR activity for the catalysts located on the M−O strong binding leg is limited by the desorption of oxygen adsorbates, and for the catalysts located on the M−O weak binding leg is limited by O_2 adsorption and the subsequent dissociation. Despite the great success of this framework in understanding and predicting the catalytic activity over a broad variety of catalysts, it normally does not account for the site-blocking effect, which describes the phenomenon of active sites being blocked by reaction intermediates and constitutes the pre-exponential term of the Arrhenius equation,[6] in spite of its apparent role in limiting ORR. As a result, the activity enhancement achieved by optimizing the metal−oxygen binding energy (ΔE) has been commonly ascribed to the improved intrinsic activity,[1,4] although some studies stated that the suppressed site-blocking effect also makes contributions.[7−9] Herein, we demonstrate the site-blocking effect and incorporate it into the activity trend framework, hereby establishing a general asymmetric volcano trend in the ORR activity of both Pt and non-Pt catalysts.

The site-blocking effect is first investigated on Fe−N−C systems as their well-defined redox chemistry and lack of side-by-side site configuration allows for quantitative evaluation of oxygen coverage. The carbon supported FePc pyrolyzed at 300 °C (FePc-300/KB) exhibits a typical profile of two redox peaks, and the one around 0.64 V (all potentials vs reversible hydrogen electrode) arises from the $Fe^{3+/2+}$ redox transition of the in-plane Fe−N_4 moiety (denoted as D2).[10] The Fe-MOF derived catalyst (detailed synthesis information is given in Supporting Information (SI)) exhibits a $Fe^{3+/2+}$ redox peak at ∼0.78 V (Figure 1), which is coupled to the out-of-plane Fe−N_4 moiety (denoted as D1) widely detected in pyrolyzed Fe−N−C catalysts.[11] The higher redox potential of D1 as compared to D2 is related to the longer Fe−N bond length that enriches the charge of the Fe center by suppressing the Fe-to-ligand back-donation.[12]

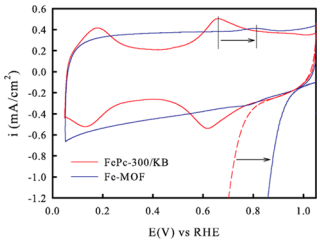

Figure 1. Cyclic voltammogram (CV) and ORR polarization plots collected for FePC-300/KB and Fe-MOF in N_2/O_2-saturated 0.1 M $HClO_4$ electrolyte at 20 mV s^{-1} at room temperature, with a rotation rate of 1,600 rpm for ORR.

Notably, both FePc-300/KB and Fe-MOF exhibit a close correlation between the redox peak and the ORR polarization curve (Figure 1). This correlation has been widely observed on both intact[13−15] and pyrolyzed Fe−N−C catalysts,[11−13,16−19]

Received: October 24, 2016
Published: January 11, 2017

DOI: 10.1021/jacs.6b11072
J. Am. Chem. Soc. XXXX, XXX, XXX−XXX

and can be accounted for by the redox mechanism pioneered by Beck and Zagal:[14−16,20,21]

$$Fe^{3+}{-}OH_{ads} + H^+ + e^- \leftrightarrow Fe^{2+} + H_2O \quad (1)$$

$$Fe^{2+} + O_2 + H^+ + e^- \rightarrow Fe^{3+}{-}OOH_{ads} \quad (2)$$

wherein the active sites for ORR are generated from the reversible redox reaction (eq 1). The unoccupied site percentage is determined by the difference between the applied potential E and the redox potential E_{redox} as described by eq 3[22]

$$1 - \Theta_O = \frac{1}{1 + e^{F/RT(E-E_{redox})}} \quad (3)$$

where Θ_O represents the OH* coverage; F is the Faraday constant; R is the universal gas constant; and T is the temperature. Interestingly, the curves of $1 - \Theta_O$ derived from eq 3 with the E_{redox} of 0.64 and 0.78 V nearly overlap the normalized ORR current density of FePc-300/KB and Fe-MOF, respectively (Figure 2a). Correspondingly, the curved Tafel plots of the catalysts closely resemble the curves of E as a function of $\ln(1 - \Theta_O)$ (Figure S1). This strongly suggests that their ORR activities are limited by the availability of active sites. As the potential scans cathodically across the E_{redox} region, more active sites become available for ORR. This accounts for the close correlation between the redox peak and the ORR polarization curve, as well as the nonlinear behavior of the Tafel plots.

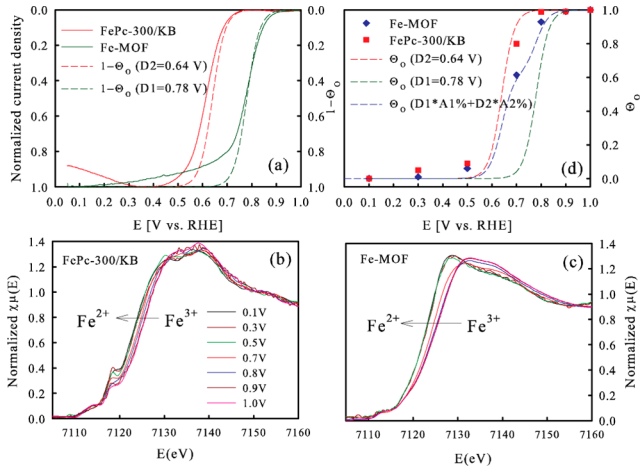

Figure 2. (a) Normalized ORR kinetic current of FePc-300/KB and Fe-MOF from Figure 1, in comparison with the Θ_O derived from eq 3 using redox potential of 0.78 V (D1) and 0.64 V (D2), respectively. *In situ* X-ray absorption near edge structure (XANES) of the FePc-300/KB (b) and Fe-MOF (c) collected at 0.1−1.0 V in N_2-saturated 0.1 M $HClO_4$ at room temperature; (d) experimental Θ_O for FePc-300/KB and Fe-MOF derived from $\Delta\mu$ analysis of the XANES (Figure S2, S3), in comparison to calculated Θ_O by using D2 or the relative content of D1 and D2 (A1% and A2%) given by Mössbauer.

The above-mentioned redox transition behavior has been directly observed for various Fe−N−C catalysts by *in situ* X-ray absorption spectroscopy (XAS),[23] which demonstrates the reversible redox reaction (eq 1) by capturing the transition from Fe^{3+} to Fe^{2+} (Figure 2b,c) associated with the removal of OH* as the potential moving across the E_{redox}. In addition, the Θ_O of FePc-300/KB follows the calculated Θ_O with a redox potential of 0.64 V; and the calculated Θ_O of Fe-MOF based on the relative content of D1 and D2 given by Mössbauer[11] matches the experimental Θ_O (Figure 2d). As expected, the Fe-MOF exhibits a much lower Θ_O than FePc-300/KB at the ORR kinetic region (Figure 2d), providing experimental evidence for the reduced Θ_O as a result of the higher E_{redox}.

In addition to suppressing the Θ_O, increasing E_{redox} also alters the turnover frequency (TOF) of $M{-}N_4$ sites since the E_{redox} of $M{-}N_4$ moieties is linearly related to the M−O binding energy (ΔE).[15] Both factors contribute to the measured kinetic current as[6,22]

$$J_{ORR}(E) \propto N_{total}(1 - \Theta_O)\exp\left(-\frac{\Delta G}{RT}\right)\exp\left(-\frac{E - E^0}{b}\right) \quad (4)$$

where $J_{ORR}(E)$ is the kinetic current obtained at the potential E; N_{total} is the total population of active sites; ΔG is the activation energy of the rate-determining step in ORR and governs the TOF at E^0; E^0 is the equilibrium potential of O_2/H_2O; and b is the value of the Tafel slope. Despite the strong coupling between $(1 - \Theta_O)$ and $\exp(-\Delta G/RT)$, their contributions to J_{ORR} can be transformed into the form of summation and thus deconvoluted by taking the logarithm on eq 4. As shown in Figure 3, the $\log(\exp(-\Delta G/RT))$ (e.g., $-\Delta G/RT$) scales linearly with ΔE[24] and thus E_{redox} on either side of the volcano (black line). Meanwhile, the $\log(1 - \Theta_O)$ increases monotonically with increasing E_{redox}, with a steep trend gradually flattened (red line). As a result, the J_{ORR} is primarily limited by $1 - \Theta_O$ at the low E_{redox} region and by TOF at the high E_{redox} region, respectively, and overall exhibits an asymmetric volcano curve as a function of E_{redox} (green line). This asymmetric volcano curve represents a general framework governing the ORR activity of Pt and non-Pt catalysts as shown next.

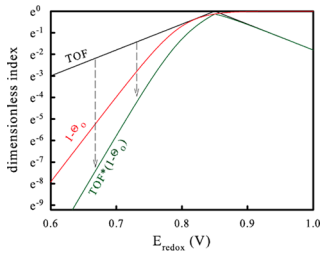

Figure 3. Plots of $(1 - \Theta_O)$ (red) as function of E_{redox} derived from eq 3 with E = 0.8 V and T = 298 K; TOF (black) represented by $\log(\exp(-\Delta G/RT))$ is rewritten as $-a|V - E_{redox}|$ with a = 12 for both sides to give a symmetric volcano curve with reasonable slopes (note that the value of a could be different on the two sides owing to different kinetics). V represents the optimized E_{redox}, which is assumed to be 0.85 V given that it is suggested to be 300−400 mV lower than the E^0 of the ORR (1.23 V),[7,22] and the $Pt_3Ni(111)$ with a E_{redox} of ∼0.85 V exhibits the highest ORR activity hitherto;[25] $(1 - \Theta_O)\exp(-12 \times |0.85 - E_{redox}|)$ (green) representing a semiempirical model combining $(1 - \Theta_O)$ and TOF. The arrows indicate the different extent of the underestimation of the TOF for active sites with different E_{redox}.

The site-blocking effect dominates catalysts with low redox potential or strong binding energy. As a result, increases in redox potential significantly contributes to improved catalytic activity. For example, a shift of E_{redox} from 0.64 to 0.78 V shows a change in surface coverage at 0.8 V by a factor of ∼170. This difference represents a significant portion of the ∼300-fold performance improvement between the FePC-300/KB and the Fe-MOF. This disagrees with current views attributing the superior ORR activity of pyrolyzed Fe−N−C catalysts to unpyrolyzed ones to

DOI: 10.1021/jacs.6b11072
J. Am. Chem. Soc. XXXX, XXX, XXX−XXX

the enhanced TOF.[1,2] This controversy is simply because although the TOF is represented by $\exp(-\Delta G/RT)$, it has been calculated by normalizing J_{ORR} with N_{total}, which gives $(1 - \Theta_O)\exp(-\Delta G/RT)$, thereby incorporating the $(1 - \Theta_O)$ into the TOF. As a result, the activity enhancement has been erroneously ascribed to the increased TOF.[4,11,21,26] Another outcome of this mis-assignment is the underestimation of the TOF, especially for active sites with low E_{redox} as indicated by the arrows in Figure 3. These arguments are in line with Zagal and Koper's[15] recent review article which pointed out that the reactivity of $M-N_4$ sites siting on the strong adsorption leg of the volcano is severely limited by the low surface concentration of M^{2+} sites, and the shape of the volcano changes upon correcting the true concentration.

The established volcano trend predicts that the activity exhibits a gradually flattened trend with E_{redox} approaching the apex because of the flattened trend of $(1 - \Theta_O)$. The prediction cannot be testified on Fe−N−C materials due to the lack of precise control over their E_{redox} in this region, but can be verified on PtM/C systems with the ΔE or E_{redox} deliberately tuned within this region by varying the M content as shown below.

Representative (solid and spherical) Pt/C, $PtCo_{0.15}$/C, and $PtCo_{0.33}$/C nanoparticle (NP) catalysts (TKK Inc.) with comparable particle size (Figure S4 and Table S1) were chosen to study the ORR activity trend within the high E_{redox} region. The Co-induced strain is confirmed by the shortened Pt−Pt bond distance (R_{PtPt}) given by extended X-ray absorption fine structure (EXAFS) analysis (Table S1 and Figure S5), which weakens ΔE or increases E_{redox}.[8,12] As a result, a dramatic anodic shift of ~65 mV in the half-wave potential ($E_{1/2}$) relative to Pt/C was obtained on $PtCo_{0.15}$/C with R_{PtPt} shortened by 0.02 Å. Further doubling the Co content shortens the R_{PtPt} by another 0.03 Å, which however only leads to a marginal shift of ~15 mV (Figure 4a), hereby confirming the flattened activity trend deduced theoretically.

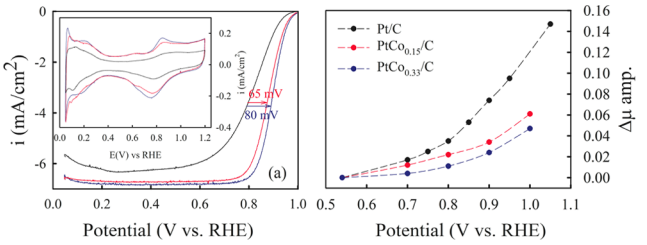

Figure 4. (a) CV (inset) and ORR polarization curves of Pt/C (black), $PtCo_{0.15}$/C (red), and $PtCo_{0.33}$/C (blue) taken in N_2/O_2-purged 0.1 M $HClO_4$ at a scan rate of 20/5 $mV \cdot s^{-1}$; (b) $|\Delta\mu|$ of the catalysts as a function of potentials derived from the Pt L_3 edge XANES spectra displayed in Figure S6.

As discussed above, the flattened activity trend is caused by the flattened $(1 - \Theta_O)$ trend arisen from the reversible redox reaction (Figure 3). The reversible redox peaks of ~0.8 V associated with water dissociation ($Pt-OH_{ads} + H^+ + e^- \leftrightarrow Pt + H_2O$)[7] are seen in the CVs of these catalysts (Figure 4a, inset). The anodic shift of the redox peak as expected from the increased E_{redox}, which has been seen on Fe−N−C systems (Figure 1) and single crystal $Pt_3M(111)$ systems,[7] is indiscernible for small PtM/C NPs[27] as seen here owing to the mixture of various facets and under-coordinated sites at the corners/edges/defects. In addition, the theoretical oxygen coverage described by eq 3 is not applicable to PtM systems due to the repulsive effect arisen from the side-by-side site configuration (Temkin isotherm).[28] Consequently, the oxygen coverage trend on PtM systems cannot be exploited by electrochemical or theoretical methods like Fe−N−C systems, but it is observable by *in situ* XAS.

In situ XAS measurements show that the Pt white line intensities for the Pt-catalysts increase monotonically with increasing potentials (Figure S6). This trend reflects the increase in oxygen coverage as it is caused by the charge transfer from the Pt surface to the oxygenated adsorbates. If assuming the Pt surface is free of adsorbates at 0.54 V (the double layer region), the relative oxygen coverage at potential E is represented by the amplitude of the subtractive $\Delta\mu(E) = \mu(E) - \mu(0.54\ V)$ (denote as $|\Delta\mu(E)|$).[8]

As shown in Figure 4b, the $|\Delta\mu(E)|$ of $PtCo_{0.15}$/C at elevated potentials is much lower than that of Pt/C, evidencing the reduced oxygen coverage caused by the Co-induced shortening of R_{PtPt} by 0.02 Å. Thus, the activity gain of ~65 mV in $E_{1/2}$ is contributed by higher $(1 - \Theta_O)$ and higher TOF combined. However, further shortening R_{PtPt} by 0.03 Å does not further reduce the oxygen coverage as the $|\Delta\mu(E)|$ of $PtCo_{0.33}$/C and $PtCo_{0.15}$/C is comparable. Thus, the corresponding activity gain of ~15 mV in $E_{1/2}$ is primarily ascribed to improved TOF. These results confirm the flattened $(1 - \Theta_O)$ trend and the resultant flattened activity trend at the high E_{redox} region.

The oxygen coverage trends with potentials of these catalysts correlates well with their Tafel plots displayed in Figure S7. The curved Tafel plot of Pt/C is typical for Pt/C electrodes[29] and attributable to the progressive growth of oxygenated adsorbates with increasing potential (Figure 4b);[30] whereas the rather straight Tafel plots of $PtCo_{0.15}$/C and $PtCo_{0.33}$/C, which are widely observed on highly active PtM/C catalysts,[31] are indicative of the suppressed oxygen species adsorption.

Similar to Fe−N−C systems, the specific activity of PtM/C catalysts is underestimated owing to the overlook of the site-blocking effect. The specific activity is defined by the mass activity normalized by the electrochemical surface area (ECSA) determined by hydrogen or copper underpotential deposition or CO stripping.[32] However, the ECSA obtained by these methods are larger than the real ECSA available for ORR at elevated potentials (such as 0.9 V) when a fraction of the ECSA is covered by oxygen species (Figure 4b). This leads to the underestimation of the specific activity, especially for small Pt/C NPs.

Lastly, it can be inferred from the framework depicted in Figure 3 that the site-blocking effect vanishes for catalysts with E_{redox} exceeding the optimal value. The ORR is thus governed by the TOF, which is limited by the overly weak ΔE. All these phenomena are observed on the representative CoPc-300/KB with a high E_{redox} of ~0.93 V (Figure 5a). The associated weak ΔE is reflected by a electron transfer number of 2.5 derived from the Koutecky−Levich plots (Figure S8), which indicates a $2e^-$ pathway dominated ORR process as widely observed for intact CoPc;[33] whereas a electron transfer number of 3.8 is obtained for Fe-MOF (Figure S9). The ORR of CoPc-300/KB occurs around 0.7 V, where the redox transition from Co^{3+} to Co^{2+} has already completed as indicated by the well-resolved redox peak and ORR polarization curve (Figure 5a). In line with the electrochemical observations, the XANES of CoPc-300/KB closely resembles that of bulk CoPc, and remains unchanged in the entire ORR range (Figure 5b). The site-blocking effect is thus ruled out, and the ORR activity of CoPc-300/KB is exclusively limited by the TOF. Overall, the ORR activity trend

DOI: 10.1021/jacs.6b11072
J. Am. Chem. Soc. XXXX, XXX, XXX−XXX

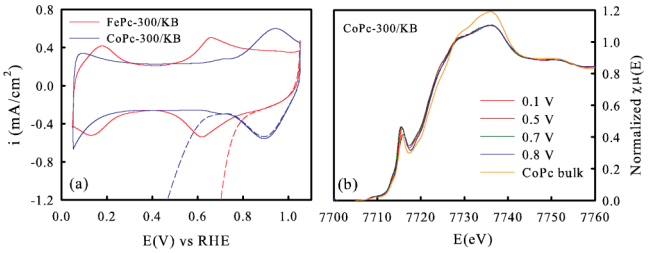

Figure 5. (a) CV and ORR polarization plots collected for FePC-300/KB and CoPc-300/KB in N_2/O_2-saturated 0.1 M $HClO_4$ electrolyte at 20 mV s^{-1} at room temperature, with a rotation rate of 1,600 rpm for ORR; (b) *in situ* XANES of CoPc-300/KB collected at 0.1−0.8 V in N_2-saturated 0.1 M $HClO_4$.

and the limiting factors have been confirmed on both sides of the volcano curve, with the two sides asymmetric due to their distinctly different ORR kinetics.

In summary, we incorporated the site-blocking effect into the activity trend framework as a function of E_{redox} or ΔE, wherein the activity is limited by the site-blocking effect and/or the intrinsic activity of active sites depending on E_{redox} or ΔE. The E_{redox} was shown to be a suitable activity descriptor that directly correlates to both ΔE and the site-blocking effect. We pointed out that the intrinsic activity of active sites with low E_{redox} or strong ΔE have been markedly underestimated due to the overlook of the site-blocking effect, and the activity enhancement achieved by increasing E_{redox} or weakening ΔE shall be attributed primarily to the suppressed site-blocking effect, rather than the improved intrinsic activity proposed hitherto. The site-blocking effect and the asymmetric volcano trend shown here are not limited to ORR but applicable to many sluggish reactions with high activation barriers.

■ ASSOCIATED CONTENT

Supporting Information

The Supporting Information is available free of charge on the ACS Publications website at DOI: 10.1021/jacs.6b11072.

Experimental details (PDF)

■ AUTHOR INFORMATION

Corresponding Author

*q.jia@neu.edu

ORCID

Jingkun Li: 0000-0003-1699-3089

Notes

The authors declare no competing financial interest.

■ ACKNOWLEDGMENTS

We appreciate financial assistance from the U.S. Department of Energy (DOE), EERE (DE-EE-0000459). This work was also supported by the Natural Science Foundation of China (21336003, 21476138). MRCAT operations are supported by the Department of Energy and the MRCAT member institution. This research used resources of the Advanced Photon Source, a DOE Office of Science User Facility operated for the DOE Office of Science by Argonne National Laboratory under Contract No. DE-AC02-06CH11357. Part of this research used ISS 8-ID beamline of the National Synchrotron Light Source II, a DOE Office of Science User Facility operated for the DOE Office of Science by Brookhaven National Laboratory under Contract No. DE-SC0012704.

■ REFERENCES

(1) Gasteiger, H. A.; Marković, N. M. *Science* **2009**, *324*, 48.
(2) Gasteiger, H. A.; Kocha, S. S.; Sompalli, B.; Wagner, F. T. *Appl. Catal., B* **2005**, *56*, 9.
(3) Jasinski, R. *Nature* **1964**, *201*, 1212.
(4) Jaouen, F. In *Non-Noble Metal Fuel Cell Catalysts*; Wiley-VCH Verlag GmbH & Co. KGaA: Weinheim, Germany, 2014; p 29.
(5) Calle-Vallejo, F.; Martinez, J. I.; Rossmeisl, J. *Phys. Chem. Chem. Phys.* **2011**, *13*, 15639.
(6) Stamenkovic, V.; Mun, B. S.; Mayrhofer, K. J.; Ross, P. N.; Markovic, N. M.; Rossmeisl, J.; Greeley, J.; Nørskov, J. K. *Angew. Chem.* **2006**, *118*, 2963.
(7) Stamenkovic, V. R.; Fowler, B.; Mun, B. S.; Wang, G.; Ross, P. N.; Lucas, C. A.; Marković, N. M. *Science* **2007**, *315*, 493.
(8) Jia, Q.; Liang, W.; Bates, M. K.; Mani, P.; Lee, W.; Mukerjee, S. *ACS Nano* **2015**, *9*, 387.
(9) Rossmeisl, J.; Karlberg, G. S.; Jaramillo, T.; Nørskov, J. K. *Faraday Discuss.* **2009**, *140*, 337.
(10) van der Putten, A.; Elzing, A.; Visscher, W.; Barendrecht, E. *J. Electroanal. Chem. Interfacial Electrochem.* **1987**, *221*, 95.
(11) Li, J.; Ghoshal, S.; Liang, W.; Sougrati, M.-T.; Jaouen, F.; Halevi, B.; McKinney, S.; McCool, G.; Ma, C.; Yuan, X.; Ma, Z.-F.; Mukerjee, S.; Jia, Q. *Energy Environ. Sci.* **2016**, *9*, 2418.
(12) Jia, Q.; Ramaswamy, N.; Hafiz, H.; Tylus, U.; Strickland, K.; Wu, G.; Barbiellini, B.; Bansil, A.; Holby, E. F.; Zelenay, P.; Mukerjee, S. *ACS Nano* **2015**, *9*, 12496.
(13) Birry, L.; Zagal, J. H.; Dodelet, J.-P. *Electrochem. Commun.* **2010**, *12*, 628.
(14) Zagal, J.; Bindra, P.; Yeager, E. *J. Electrochem. Soc.* **1980**, *127*, 1506.
(15) Zagal, J. H.; Koper, M. *Angew. Chem., Int. Ed.* **2016**, *55*, 14510.
(16) Tylus, U.; Jia, Q.; Strickland, K.; Ramaswamy, N.; Serov, A.; Atanassov, P.; Mukerjee, S. *J. Phys. Chem. C* **2014**, *118*, 8999.
(17) Van Veen, J. R.; van Baar, J. F.; Kroese, K. J. *J. Chem. Soc., Faraday Trans. 1* **1981**, *77*, 2827.
(18) Zagal, J. H.; Ponce, I.; Baez, D.; Venegas, R.; Pavez, J.; Paez, M.; Gulppi, M. *Electrochem. Solid-State Lett.* **2012**, *15*, B90.
(19) van Veen, J. A. R.; Colijn, H. A.; van Baar, J. F. *Electrochim. Acta* **1988**, *33*, 801.
(20) Beck, F. J. *J. Appl. Electrochem.* **1977**, *7*, 239.
(21) Ramaswamy, N.; Tylus, U.; Jia, Q.; Mukerjee, S. *J. Am. Chem. Soc.* **2013**, *135*, 15443.
(22) Gottesfeld, S. *ECS Trans.* **2014**, *61*, 1.
(23) Jia, Q. *Nano Energy* **2016**, *29*, 65.
(24) Nørskov, J. K.; Rossmeisl, J.; Logadottir, A.; Lindqvist, L.; Kitchin, J. R.; Bligaard, T.; Jonsson, H. *J. Phys. Chem. B* **2004**, *108*, 17886.
(25) Stephens, I. E. L.; Bondarenko, A. S.; Gronbjerg, U.; Rossmeisl, J.; Chorkendorff, I. *Energy Environ. Sci.* **2012**, *5*, 6744.
(26) Sahraie, N. R.; Kramm, U. I.; Steinberg, J.; Zhang, Y.; Thomas, A.; Reier, T.; Paraknowitsch, J.-P.; Strasser, P. *Nat. Commun.* **2015**, *6*, 8618.
(27) Dubau, L.; Nelayah, J.; Moldovan, S.; Ersen, O.; Bordet, P.; Drnec, J.; Asset, T.; Chattot, R.; Maillard, F. *ACS Catal.* **2016**, *6*, 4673.
(28) Temkin, M. I. *Zh. Fiz. Chim* **1941**, *15*, 296.
(29) Paulus, U. *J. Phys. Chem. B* **2002**, *106*, 4181.
(30) Subramanian, N.; Greszler, T.; Zhang, J.; Gu, W.; Makharia, R. *J. Electrochem. Soc.* **2012**, *159*, B531.
(31) Huang, X. *Science* **2015**, *348*, 1230.
(32) Shao, M.; Odell, J. H.; Choi, S.-I.; Xia, Y. *Electrochem. Commun.* **2013**, *31*, 46.
(33) Van Der Putten, A.; Elzing, A.; Visscher, W.; Barendrecht, E. *J. Electroanal. Chem. Interfacial Electrochem.* **1986**, *214*, 523.

DOI: 10.1021/jacs.6b11072
J. Am. Chem. Soc. XXXX, XXX, XXX−XXX